sustainability

MDPI

Article

Antifungal Activity of Ag and ZnO Nanoparticles Co-Loaded in Zinc–Alginate Microparticles

Marko Vinceković [1,*], Lana Živković Genzić [1], Nenad Jalšenjak [1], Joško Kaliterna [2], Iva Rezić Meštrović [3], Mislav Majdak [3], Suzana Šegota [4], Marijan Marciuš [5], Lidija Svečnjak [6], Ivica Kos [7], Ivona Švenda [1] and Katarina Martinko [2]

[1] Division of Agroecology, Department of Chemistry, Faculty of Agriculture, University of Zagreb, Svetošimunska Cesta 25, 10000 Zagreb, Croatia; lzivkovic@agr.hr (L.Ž.G.); njalsenjak@agr.hr (N.J.); ivonasvenda@live.com (I.Š.)
[2] Division of Phytomedicine, Department of Plant Pathology, Faculty of Agriculture, University of Zagreb, Svetošimunska Cesta 25, 10000 Zagreb, Croatia; jkaliterna@agr.hr (J.K.); kmartinko@agr.hr (K.M.)
[3] Department of Applied Chemistry, Faculty of Textile Technology, University of Zagreb, Prilaz Baruna Filipovića 28a, 10000 Zagreb, Croatia; iva.rezic@ttf.unizg.hr (I.R.M.); majdak.mislav@gmail.com (M.M.)
[4] Laboratory for Biocolloids and Surface Chemistry, Ruđer Bošković Institute, Bijenička c. 54, 10000 Zagreb, Croatia; ssegota@irb.hr
[5] Division of Materials Chemistry, Ruđer Bošković Institute, Bijenička Cesta 54, 10000 Zagreb, Croatia; marijan.marcius@irb.hr
[6] Division of Animal Science, Department of Fisheries, Apiculture, Wildlife Management and Special Zoology, Faculty of Agriculture, University of Zagreb, Svetošimunska Cesta 25, 10000 Zagreb, Croatia; lsvecnjak@agr.hr
[7] Division of Animal Science, Department of Animal Science and Technology, Faculty of Agriculture, University of Zagreb, Svetošimunska Cesta 25, 10000 Zagreb, Croatia; ikos@agr.hr
* Correspondence: mvincekovic@agr.hr; Tel.: +385-1-239-3953

Abstract

Fungal infections caused by *Fusarium solani* demand sustainable alternatives to conventional fungicides and free nanoparticles, which often show poor stability and rapid release. This study developed zinc-crosslinked alginate microparticles containing silver (AgNPs), zinc oxide (ZnONPs), or both to improve nanoparticle stability, sustain release, and enhance antifungal efficacy. Microparticles were produced by ionic gelation and characterized by FTIR, microscopy, swelling analysis, encapsulation efficiency, and kinetic modeling. AgNPs weakened hydrogen bonding within alginate, yielding rough, porous structures, whereas ZnONPs strengthened COO^{-}–Zn^{2+} interactions, forming smoother surfaces with smaller pores; co-loaded particles combined both characteristics. Encapsulation efficiencies were 77.9% (AgNPs) and 98.6% (ZnONPs), with co-loaded systems retaining 64.0% and 98.9%, respectively. Swelling was highest in AgNP-loaded microparticles (63.8%) and lowest in ZnONP and co-loaded systems (≈42%). AgNPs followed anomalous transport (n = 0.65), while ZnONPs transitioned from Fickian diffusion ($n \approx$ 0.36–0.38) to zero-order release (K_0 = 1.00 for ZnONPs alone; 0.80 co-loaded). Antifungal tests showed strong inhibition: 80.7% for AgNPs, 91.4% for ZnONPs, and 99.7% for co-loaded formulations. Microscopy confirmed membrane disruption, hyphal collapse, and ROS-mediated damage, with the strongest effects in co-loaded samples. These results demonstrate a tunable, synergistic, sustained-release platform that outperforms single nanoparticles and offers a promising strategy for sustainable crop protection.

Keywords: zinc–alginate; silver nanoparticles; zinc oxide nanoparticles; sustained release; antifungal activity (*Fusarium solani*)

Academic Editor: Haiming Zhao

Received: 1 November 2025
Revised: 9 December 2025
Accepted: 12 December 2025
Published: 18 December 2025

Citation: Vinceković, M.; Živković Genzić, L.; Jalšenjak, N.; Kaliterna, J.; Rezić Meštrović, I.; Majdak, M.; Šegota, S.; Marciuš, M.; Svečnjak, L.; Kos, I.; et al. Antifungal Activity of Ag and ZnO Nanoparticles Co-Loaded in Zinc–Alginate Microparticles. *Sustainability* **2025**, *17*, 11374. https://doi.org/10.3390/su172411374

1. Introduction

Fungal infections continue to undermine global agricultural productivity, threatening food security and necessitating antifungal strategies that combine long-term efficacy with reduced environmental impact [1,2]. Metal and metal oxide nanoparticles (NPs), particularly silver (AgNPs) and zinc oxide (ZnONPs), have received considerable attention owing to their broad-spectrum antimicrobial activity, their capacity to disrupt microbial membranes, and their ability to generate reactive oxygen species (ROS) that damage essential cellular components [3–6]. However, despite their potency, the direct use of free nanoparticles in agricultural systems is constrained by rapid aggregation, uncontrolled or burst release, limited persistence, and the risk of off-target toxicity. These limitations underscore the need for advanced delivery platforms capable of stabilizing nanoparticles, improving their bioavailability, and enabling controlled and sustained release at the infection site [7–9]. Biopolymer-based matrices, especially alginate hydrogels and microparticles, offer promising solutions due to their biocompatibility, facile gelation with divalent cations, tunable porosity, and ability to protect sensitive bioactive agents from degradation [10,11]. Zinc-crosslinked alginate is particularly attractive, as Zn^{2+} not only contributes antimicrobial functionality but also establishes specific coordination interactions (COO^{-}–Zn^{2+}) that modify network architecture, swelling capacity, and release profiles [12,13]. Alginate microparticles have therefore been widely used to encapsulate small molecules, enzymes, and nanoparticles, with loading efficiency and release behavior modulated through crosslinking density, particle size, and drying method [14–16].

Nanoparticles (≈1–100 nm) differ fundamentally from microparticles (≈1–1000 μm) in size-dependent properties and biological behavior. At the nanoscale, high surface-to-volume ratios and interfacial effects enhance reactivity, diffusion, and cell/biofilm interactions, enabling deeper matrix penetration and faster transport or release [17–22]. In our system, AgNPs (~45–50 nm) and ZnONPs (~110 nm rods) exhibit strong surface-driven interactions with alginate, modifying crosslinking and swelling, while alginate microparticles are spherical carriers hundreds to thousands of μm in size that provide bulk, sustained release, and practical handling [23–30]. This nano–micro distinction underpins the co-loading design and the observed antifungal outcomes [10,31–35].

AgNPs and ZnONPs exhibit distinct yet complementary antimicrobial mechanisms—AgNPs disrupt cell membranes and interact with proteins and nucleic acids, whereas ZnONPs induce toxicity through ion dissolution, ROS generation, and photocatalytic activity [36–41]. Co-loading these nanoparticles within a single carrier could harness additive or synergistic effects, enhance antifungal performance, and reduce the concentrations required for efficacy. Nevertheless, several unresolved challenges limit the rational design of such integrated systems. First, most existing studies examine free nanoparticles, despite their known instability and inconsistent antifungal outcomes in agricultural contexts [7–9]. Second, the influence of nanoparticles with differing sizes, shapes, and surface chemistries on zinc–alginate crosslinking, network organization, and transport phenomena remains insufficiently understood, even though these parameters critically determine release kinetics and biological performance [42–44]. Third, research on co-loaded nanoparticle systems in polysaccharide matrices is scarce, leaving uncertain how multi-nanoparticle interactions alter microparticle morphology, porosity, and diffusional pathways [45–47]. Finally, while *Fusarium solani* is a highly virulent and economically significant phytopathogen affecting a wide range of crops [48,49], few studies have directly linked nanoparticle–matrix structural characteristics to quantifiable antifungal effects against this species.

To address these gaps, the present study hypothesizes that co-loading silver (AgNPs) and zinc oxide nanoparticles (ZnONPs) into zinc-crosslinked alginate microparticles will yield a structurally optimized, synergistic, and sustained-release antifungal system that out-

performs single-nanoparticle formulations while reducing environmental impact through controlled delivery and minimized nanoparticle dispersion. To test this hypothesis, the study pursues the following specific objectives:

(1) Prepare zinc-crosslinked alginate (ALG/Zn) microparticles encapsulating AgNPs, ZnONPs, or their combination;

(2) Characterize nanoparticle–matrix molecular interactions, microparticle morphology, swelling behavior, and release kinetics;

(3) Assess the antifungal efficacy of each formulation against the phytopathogenic fungus *F. solani*;

(4) Link structural and kinetic properties with antifungal performance, establishing design principles for sustainable nanoparticle-based crop protection platforms.

Spectroscopic and microscopic analyses elucidate nanoparticle–matrix interactions and morphological features, while swelling behavior and kinetic modeling provide insight into transport mechanisms. Antifungal assays against *F. solani* establish how co-loading influences biological performance. By integrating structural, kinetic, and biological data, this work advances the design of sustained-release, synergistic nanoparticle-based antifungal platforms and contributes formulation principles relevant to sustainable crop protection.

2. Materials and Methods

2.1. Materials

Low-viscosity sodium alginate (CAS Number: 9005-38-3; Brookfield viscosity 4–12 cps (1% in H_2O at 25 °C)) was purchased from Sigma Aldrich (Burlington, VT, USA), zinc sulfate heptahydrate (CAS Number: 7446-20-0) was purchased from Gram-Mol d.o.o. (Zagreb, Croatia), silver nanoparticles (AgNPs) (CAS Number: 7440-22-4, 50 wt.%, dispersion in tripropylene glycol mono methyl ether) were purchased from Sigma Aldrich, and zinc oxide nanoparticles (ZnONPs, 2.5 wt.%, viscosity 2.8 cP, work function 4.3 eV) (CAS Number: 1314-13-2) were purchased from Sigma Aldrich. All other chemicals were of analytical grade and used as received without further purification.

2.1.1. Preparation of ALG/Zn Microparticles and Formulations with AgNPs, ZnONPs, or a Mixture of AgNPs + ZnONPs

ALG/Zn microparticles and formulations with AgNPs (Formulation 1), ZnONPs (Formulation 2), or a mixture of AgNPs + ZnONPs (Formulation 3) were prepared by ionic gelation as previously described [50]. First, 100 mL of 2% sodium alginate solution was mixed with 5 mL of AgNPs, ZnONPs, or a combination thereof, and the mixture was then dropped into an equal volume of 2% zinc sulfate heptahydrate solution through a 360 µm nozzle at 2000 Hz and 555 mbar (Büchi-B390, Büchi Labortechnik AG, Flawil, Switzerland). The resulting microparticles had initial molar concentrations of Zn (0.69 mmol/dm^3), AgNPs (0.397 mmol/dm^3), and ZnONPs (0.687 mmol/dm^3) and were mixed on a magnetic stirrer (IKA topolino, Staufen im Breisgau, Germany). The microparticles were stirred in the crosslinking solution for 30 min, filtered, washed three times with distilled water, and stored at 4 °C. Formulations were prepared to isolate the contribution of each nanoparticle and their combined effect: Formulation 1 particles to assess silver-driven activity, Formulation 2 particles to evaluate zinc oxide behavior, and Formulation 3 particles to determine whether combining both nanoparticles enhances structural properties and antifungal efficacy.

2.1.2. Isolation and Identification of *Fusarium solani*

The pathogenic fungus Fusarium solani isolate used in the experiment was morphologically identified according to Leslie and Summerell [50]. The species was originally

isolated from potato tubers with symptoms of dry rot. After isolation into a pure culture, the isolate was cultivated on PDA and incubated at 24 °C in a dark climate chamber.

2.2. Methods

2.2.1. Attenuated Total Reflectance Fourier Transform Infrared Spectroscopy (ATR-FTIR)

All samples were analyzed by Fourier transform infrared spectroscopy (FTIR) coupled with the attenuated total reflectance (ATR) recording technique. FTIR-ATR spectra of the samples were acquired using the Cary 660 FTIR spectrometer (Agilent Technologies, Palo Alto, CA, USA) and the Golden Gate single-reflection diamond ATR accessory (Specac). Spectra were recorded in the mid-infrared region (spectral range: 4000–400 cm^{-1}) and transmission mode. Prior to spectral analysis, the materials were pulverized to a fine homogenate using a porcelain mortar. To produce the FTIR-ATR spectrum of a thin uniform layer of each sample, approximately 10 mg was pushed onto a diamond ATR plate with a self-leveling sapphire anvil. Each sample had two replicate scans per spectrum, which were obtained with different aliquots. Spectra were collected at a nominal resolution of 4 cm^{-1} and room temperature (24 ± 2 °C). Raw spectral data were stored and pre-analyzed using the Agilent Resolutions Pro version 5.3.0 software package (Agilent Technologies, Palo Alto, CA, USA), with additional spectral data analysis and processing performed using the optical spectroscopy software Spectragryph (version 1.2.16.1) and Origin 8.1 (Origin Lab Corporation, Northampton, MA, USA).

2.2.2. Physicochemical Characterization of Formulations

(a) The encapsulation efficiency (EE) was estimated using the Xue et al. [51] technique based on the starting concentration of AgNPs and ZnONPs (c_{tot}) and the amount of AgNPs and ZnONPs in dry formulations (c_{load}). Encapsulation efficiency is stated as a percentage of total AgNPs and ZnONPs (c_{tot}) and computed using the following equation:

$$EE/\% = (C_{load}/C_{tot}) \times 100, \quad (1)$$

where $C_{load} = C_{tot} - c_f$, and c_f is the concentration of AgNPs and ZnONPs in the filtrate.

(b) To determine the loading capacity (LC) of AgNPs or ZnONPs in formulations, 4 g of dry microparticles were dispersed in 25 mL of a mixture of 17.65 g (0.06 mol dm^{-3}) $Na_3C_6H_5O_7 \cdot 2H_2O$ at pH 8 and 16.80 g (0.2 mol dm^{-3}) $NaHCO_3$. A magnetic stirrer (IKA Topolino, Staufen im Breisgau, Germany) was used to mix the dispersion at 400 rpm until all the microparticles had been dissolved. The concentrations of Ag and ZnO nanoparticles in the filtrate were measured after the solution was filtered through a double mus. The loading capacity was determined using the following formula and is expressed as the amount of AgNPs or ZnONPs in moles per 1 g of dry microparticles:

$$LC = (C_{NPs} \times V/W_c), \quad (2)$$

where C_{NPs} is the concentration of AgNPs or ZnONPs in the sample, V is the volume of the sample, and w_c is the weight of the microparticles.

(c) Dry microparticles (0.1 g) were dispersed in a glass vial with 10 mL of deionized water to create samples for determining the degree of swelling (S_w). The samples were then left to swell for three hours at room temperature. After blotting the swollen microparticles with filter paper to remove any surface moisture, they were weighed immediately to determine their wet weight [52]. The following formula was used to determine the swelling degree:

$$S_w = (w_t - w_0)/w_0) \times 100, \quad (3)$$

where w_t is the weight of the swollen microparticles, and w_0 is their initial weight.

(d) In vitro release of AgNPs or ZnONPs from formulations was investigated by dispersing 8 g of microparticles in 100 mL of deionized water and allowing them to stand at room temperature without stirring. At regular intervals, the dispersion was agitated for 60 s, aliquots were taken, and the amount of AgNPs or ZnONPs released was measured using a UV/VIS spectrophotometer (Shimadzu, UV-1700, Kyoto, Japan) at λ_{max}(AgNPs) = 420 nm and λ_{max}(ZnONPs) = 370 nm.

$$f_{NPs} = R_t / R_{tot}, \quad (4)$$

where f represents the fraction of released AgNPs (f_{AgNPs}) or ZnONPs (f_{ZnONPs}), R_t is the amount of AgNPs or ZnONPs released at time t, and R_{tot} is the total amount of AgNPs or ZnONPs in formulations. The standard deviation of the kinetic release parameters was calculated from the fitted curves using Origin (Pro) 9.1 (Northampton, MA, USA).

(e) All experiments were repeated three times, and the data are presented as mean values and standard deviations. Data corresponding to a normal distribution were analyzed by one-way analysis of variance (one-way ANOVA).

2.2.3. Microscopic Observations

The morphology, size, and shape of ALG/Zn microparticles and Formulation 2, 3, and 3 were analyzed by optical (OM) (Leica MZ16a stereo microscope, Leica Microsystems Ltd., Balgach, Switzerland) and scanning electron microscope (SEM) (FE-SEM, model JSM-7000F, Jeol Ltd., Tokyo, Japan) The average diameter of wet and dry microparticles was calculated by OM utilizing Olympus Soft Imaging Solutions GmbH (version E_LCmicro_09Oct2009). To determine the size distribution, twenty microparticles were randomly picked from batches generated in triplicate. Samples for SEM analysis were placed on highly conductive graphite tape. The FE-SEM was linked to an EDS/INCA 350 (energy-dispersive X-ray analyzer) developed by Oxford Instruments Ltd. (Oxford, UK).

The size, shape, and morphology of AgNPs and ZnONPs were analyzed by scanning electron microscope (SEM) (FE-SEM, model JSM-7000F, Jeol Ltd., Tokyo, Japan) and atomic force microscope (AFM) (MultiMode Scanning Probe Microscope with Nanoscope IIIa controller, Bruker, Billerica, MA, USA). The AFM laser spot was positioned at the end of the cantilever. All samples are imaged in Tapping Mode under ambient conditions in air using an R-TESPA 300 probe (Bruker, Billerica, MA, USA) at a Nom. Freq. of 300 kHz and a Nom. Spring constant of 40 N/m. The tapping force was maintained at a low level (0.8–0.9), which is appropriate for studying soft and deformable nanoparticles. The linear scanning rate was optimized between 1.0 and 1.48 Hz at a scan angle of 90°. The imaging and data collection were performed using a 256-pixel array (256 × 256). Two types of data were collected: height and amplitude. The analysis of the image was performed using the offline AFM NanoScopeTM software (Digital Instruments, Santa Barbara, CA, USA, Version V614r1 and V531r1). All images are presented as raw data except for the first-order two-dimensional flattening. The dimensions of nanoparticles were determined by cross-section analysis and by particle analysis in an imaged area (2 μm × 2 μm) containing at least 100 nanoparticles using the particle analysis option within the AFM NanoScope Control software, version V531r1. A minimum nanoparticle height of 1 nm was set. The summary table was reported to contain the number of particles analyzed, the minimum and maximum particle sizes, the average nanoparticle height, and the standard deviation.

A representative sample (10 mL) of the diluted nanoparticle suspension (2 mg/mL) was prepared. First, 4 μL of the diluted nanoparticle suspension was deposited directly onto the freshly cleaved mica (Mica Grade V-4, 9.9 mm disc) mounted on the SPM Sample Mounting Disc. After 70 s, the mica surface was washed with 200 μL Milli-Q water to remove unabsorbed nanoparticles. The washing procedure was repeated four times. The

mica surface was left to dry in air for 4 h. All samples were prepared using the same method and imaging procedure under the same ambient conditions.

2.2.4. Testing the Antifungal Effect of Novel Formulations on *Fusarium solani*

The antifungal effect of the novel formulation was investigated using the poisoned-food method, as modified by Sahar and Ouda (2014) [53]. For the experiment, 1 mg of microparticles per Petri plate (corresponding to 0.1 mg/mL in 10 mL PDA) was applied to the bottom of sterile Petri dishes, which were then immersed in 10 mL of PDA medium (50 °C). Using circular movements, the microparticles were evenly distributed in the PDA medium, which was then left to cool. A mycelial disc of *F. solani*, cut from a 7-day-old pure culture, was inoculated into the center of a cooled PDA containing formulations (test Petri dish). Control Petri dishes contained only a mycelial disc of *F. solani* inoculated on PDA medium without formulations. The experiment for each formulation was set up in five replicates. The test and control Petri dishes were incubated for seven days in the dark at 24 °C. After 7 days, photographs of the test and control Petri dishes were processed using the ImageJ software 1.54p, according to the modified method of Martinko et al. (2022) [54]. Based on the pathogen inhibition index, the degree of antifungal activity (%) was assessed. All data were statistically analyzed using one-way ANOVA followed by Tukey's post hoc test ($p < 0.05$). Results are expressed as mean inhibition ± standard deviation (SD) in SPSS 26.0.

3. Results and Discussion

The results are presented and discussed in two parts. In the first part, the characterization of the prepared ALG/Zn loaded with Ag and ZnO nanoparticles is analyzed. In the second part, the influence of novel formulations on the phytopathogenic fungus *Fusarium solani* is evaluated.

3.1. Identification of Molecular Interactions Between Formulations Constituents

The FTIR spectra of the individual nanoparticles (Figure 1a) and the alginate-based microparticles and formulations (Figure 1b) confirm that the nanoparticles interact with the alginate matrix mainly through non-covalent coordination and hydrogen bonding, without the formation of new covalent bonds. For citrate-stabilized AgNPs, the bands at 3336 cm^{-1} (O–H) and 1636 cm^{-1} (citrate C=O) match typical spectra of aqueous citrate-capped AgNPs [53,55,56]. ZnONPs show features at 3323, 2365, 1613, 1469, 1069, and 628 cm^{-1}, including the Zn–O band at 1069 cm^{-1}, consistent with established ZnO assignments and their known sensitivity to synthesis and surface residues [57–60]. Sodium alginate displays the expected O–H and COO^- vibrations at 3445, 1630, and 1445 cm^{-1}. After crosslinking with Zn^{2+}, these bands shift and broaden due to coordination between Zn^{2+} and alginate carboxylates, consistent with previous reports for Zn–alginate systems [23,61]. The broader, more intense O–H band in ALG/Zn microparticles indicates strengthened hydrogen bonding and higher network polarization, in agreement with typical spectral changes induced by divalent-cation crosslinking [23,61,62]. Comparing the formulations, no new peaks appear, confirming the absence of covalent modification. Instead, spectral differences reflect changes in hydrogen bonding and ionic coordination: Formulation 1 (AgNP-loaded) shows decreased intensity and narrowing of the O–H and COO^- bands, indicating weakened hydrogen bonding and reduced electrostatic association within the alginate network. This aligns with the disruptive effect of negatively charged citrate-stabilized AgNPs in polysaccharide gels [23,63]. Formulations 2 and 3 (ZnONP-loaded) show increased intensity and broadening of O–H and COO^- bands (≈1590 and 1407 cm^{-1}), demonstrating enhanced hydrogen bonding and stronger alginate–Zn coordination, including formation of COO–Zn complexes [23,61,62,64]. The effect is stronger in Formulation

2, while co-loading with AgNPs (Formulation 3) slightly attenuates this strengthening, suggesting competition between ZnONPs and AgNPs for interaction with the polymer.

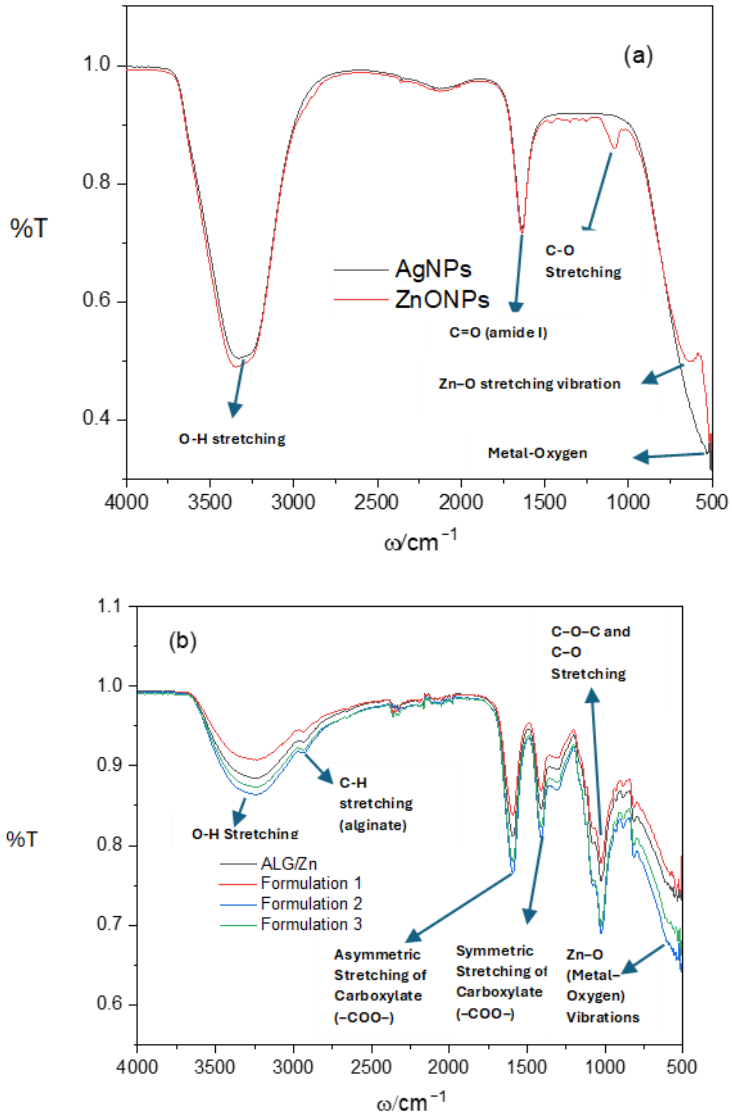

Figure 1. FTIR spectrum of (**a**) single components AgNPs (black line) and ZnONPs (red line), and (**b**) ALG/Zn microparticles (black line) and Formulation 1 (red line), Formulation 2 (blue line), and Formulation 3 (green line). The functional groups are highlighted in (**a**,**b**).

Overall, the FTIR data indicate that ZnONPs reinforce the alginate network through stronger ionic coordination and hydrogen bonding, whereas citrate-stabilized AgNPs weaken these interactions, thereby loosening the network. These spectroscopic trends correlate with the observed structural and release behaviors: ZnONP-containing microparticles form tighter, more compact networks, associated with slower Zn^{2+}/ZnO release, whereas AgNP-loaded systems exhibit more open structures, consistent with faster early Ag release. This complementary behavior agrees with previous reports and supports the design of mixed-nanoparticle systems with tunable, synergistic antifungal performance [23,53,64].

3.2. Microscopic Analyses

3.2.1. Size, Shape, and Morphology of AgNPs and ZnONPs

The SEM micrographs and size distributions (Figure 2) show that the synthesized AgNPs are predominantly spherical to quasi-spherical with smooth, rounded outlines and a fairly monodisperse population (average diameter ≈ 45–50 nm), with only a mi-

nor fraction displaying weak faceting attributable to crystalline silver facets; locally, the particles form close-packed domains with short-range hexagonal ordering but also less dense regions, a morphology consistent with homogeneous nucleation of citrate-stabilized AgNPs reported elsewhere [17,18,64]. In contrast, ZnONPs assemble into densely agglomerated, polydisperse collections of faceted crystallites and short rod-/pillar-like particles (mean rod length ≈ 110 nm), often showing sintering/stacking contacts and a rough, granular surface suggestive of polycrystalline substructure—features that agree with hydrothermal/solution or vapor-grown ZnO morphologies described in the literature [19,20]. EDX indicates that AgNP samples also carry S, C, O, and Na surface species (likely residual citrate or adventitious carbon/adsorbates), while ZnONPs show C and O consistent with surface modification/adsorbed hydroxyl/carbonaceous species after synthesis; such surface residues are commonly observed and are known to influence colloidal stability, particle–matrix interactions, and biological activity. Together, the contrasted shapes and surface textures explain key functional differences: the small, smooth, nearly spherical AgNPs are expected to diffuse more readily and embed deeper into alginate matrices, whereas larger, faceted/rod-like ZnO particles with rough surfaces promote stronger surface interactions and mechanical interlocking with the polymer network.

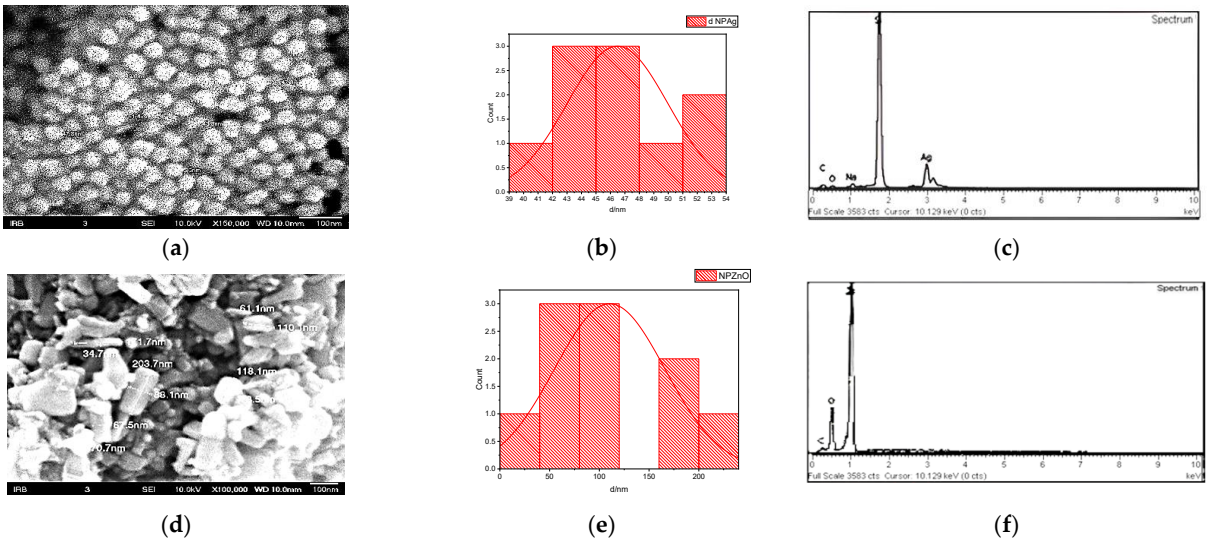

Figure 2. SEM microphotographs of AgNPs (**a**) and ZnONPs (**d**). The scale bars are indicated. Size distribution of AgNPs (**b**) and ZnONPs (**e**). Surface elemental analysis using dispersive X-ray spectroscopy (EDX) of AgNPs (**c**) and ZnONPs (**f**).

AFM analysis of AgNPs and ZnONPs (Table 1, Figure 3) was performed on monolayers adsorbed to freshly cleaved mica and evaluated using height data (minimum height threshold 1 nm) to avoid lateral-tip broadening artifacts. The amplitude/topography images show predominantly spherical, symmetric single particles with no evidence of multi-layer aggregation under the chosen sample preparation, confirming that the measured heights reflect individual nanoparticles rather than clusters. AgNP suspensions were stable but showed a broad height distribution (1–54 nm; mean height 3.5 ± 5.9 nm), whereas ZnONP suspensions were more narrowly distributed (1–8 nm; mean height 3.5 ± 2.0 nm), indicating a tighter size population on mica for ZnO (Table 1). The much smaller AFM heights versus SEM diameters reflect the different sample states and measurement principles (AFM measures particle height on a wet-deposited monolayer; SEM reports projected diameters of dried powders). Importantly, the wide AFM height spread for Ag-NPs—in contrast with the relatively monodisperse SEM diameters—suggests a bimodal behavior in the colloid. This behavior indicates a dominant population of very low-profile, likely

flattened or partially dried particles on mica, plus a minority of taller particles (possibly small aggregates or crystallographically faceted individuals). This pattern has previously been observed for citrate-capped Ag colloids, where adsorption, capillary forces, and ligand shell differences alter particle profile on substrates [17,18,64]. By contrast, the narrow ZnO height distribution and low standard deviation imply stronger colloidal homogeneity and/or a more rigid surface chemistry that limits deformation upon adsorption, consistent with reports of hydrothermally synthesized ZnO showing narrow nanoscale thicknesses in AFM studies [19,20]. These AFM results provide a practical explanation for functional differences: the small, substrate-flattened AgNP fraction tends to penetrate and diffuse differently in alginate matrices than the stiffer, more uniform ZnONPs, which helps rationalize the distinct swelling/release and embedding depths observed in the microparticles.

Table 1. Evaluated data of the average particle height/nm of the single nanoparticles of AgNPs and ZnONPs.

Nanoparticles	Number of Analyzed Particles	Average Particle Height/nm	Standard Deviation/nm
AgNPs	373	3.5	5.9
ZnONPs	140	3.5	2.0

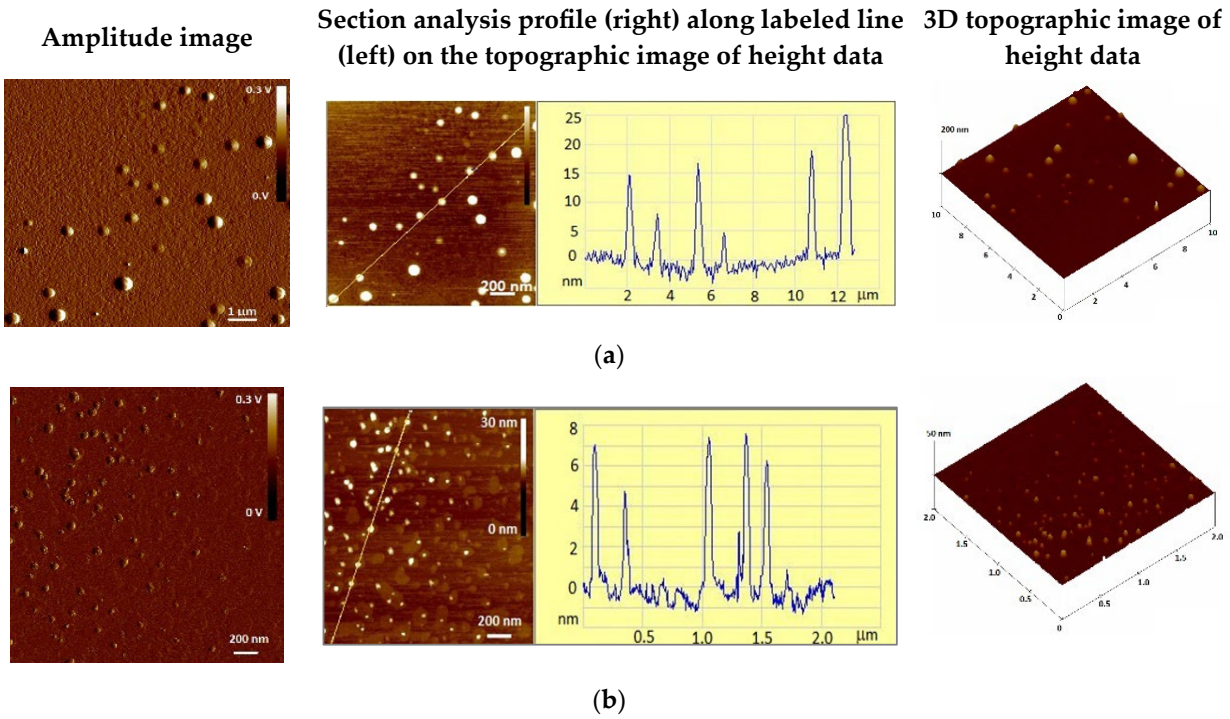

Figure 3. Amplitude image, section analysis profile (**right**) along labeled line (**left**) on the topographic image of height data, and 3D topographic image of height data of AgNPs (**a**) and ZnONPs (**b**).

3.2.2. Morphological Properties of Microparticles

The morphological and structural differences observed among the formulations reflect how AgNPs and ZnONPs modulate the organization of the alginate network during ionotropic gelation and subsequent drying. The larger pores and rougher, more heterogeneous surfaces of Ag-containing microparticles indicate that AgNP incorporation disrupts local gel uniformity and reduces the effective crosslinking density, likely due to nanoparticle aggregation or partial competition with divalent ions for alginate binding sites, a phenomenon also reported for Ag–alginate composites in previous studies [22,24,25]. In contrast, the smoother, more compact surfaces and smaller pores measured in ZnO-loaded microparticles are consistent with reports showing strong ionic interactions between

Zn^{2+}/ZnO surfaces and alginate carboxylate groups, which increase network rigidity and reduce free volume within the hydrogel matrix [26–28]. The pore sizes obtained in this study (~100–183 nm) fall within the general range reported for dried ionotropically gelled alginate materials, where capillary stresses during solvent removal typically generate nanometric porous structures [29,60]. The comparatively minimal deformation of Formulation 3 during drying and its intermediate pore size suggest a structural balance between the Ag-induced loosening of the polymer network and the ZnO-induced reinforcement of crosslinking domains. Overall, these results align with established correlations between nanoparticle type, crosslinking density, and mass-transport behavior in alginate microgels, indicating that AgNP-containing matrices may support faster or more burst-like release, while ZnO-containing systems are expected to enable slower, more sustained release profiles [21,22,26]. The size, shape, morphology, and surface of the prepared formulations are presented in Figure 4, and the size distribution of the prepared formulations is presented in Figure 5.

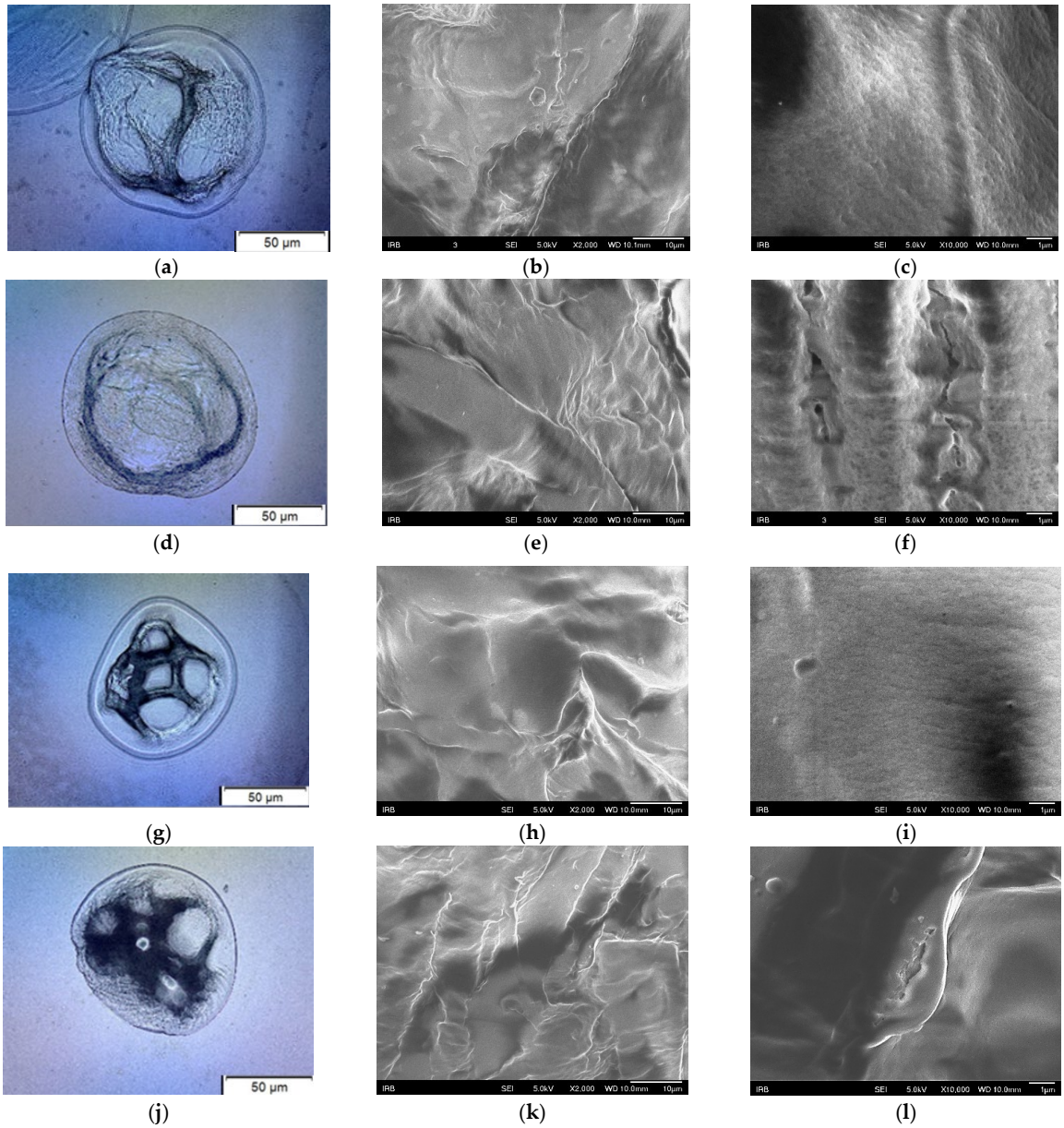

Figure 4. OM and SEM microphotographs of ALG/Zn (**a**–**c**), Formulation 1 (**d**–**f**), Formulation 2 (**g**–**i**), and Formulation 3 (**j**–**l**). The scale bars are marked on each image.

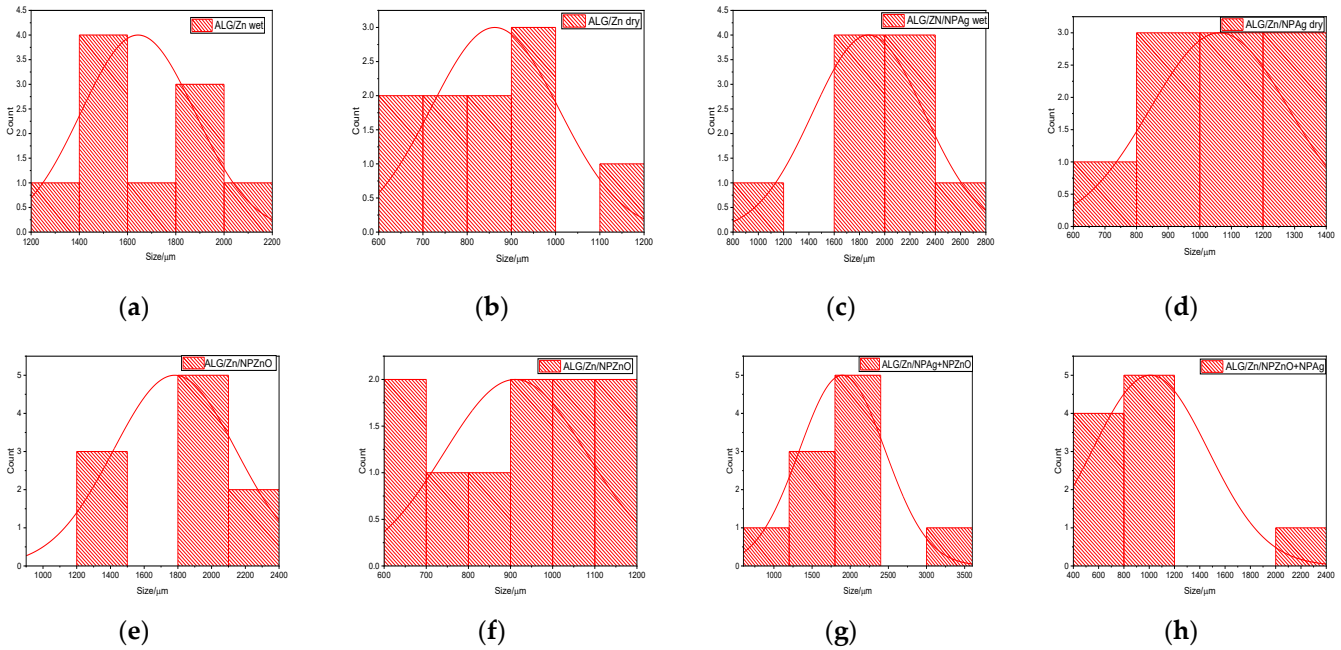

Figure 5. The size distributions of wet (**a**,**c**,**e**,**g**) and dry microparticles (**b**,**d**,**f**,**h**). ALG/Zn (**a**,**b**), Formulation 1 (**c**,**d**), Formulation 2 (**e**,**f**), and Formulation 3 (**g**,**h**).

Tables 2 and 3 present the means and variances for the wet and dry formulations across Formulation 2, Formulation 3, Formulation 1, and ALG/Zn. The ANOVA results indicate significant differences among the group means, with an F-statistic of 7.91 and a *p*-value of < 0.0001. This suggests that the formulation type significantly affects the measured outcomes.

Table 2. Means and Variances of Wet and Dry Formulations.

Formulations	Mean (Wet)/μm	Variance (Wet))/μm	Mean (Dry)/)/μm	Variance (Dry))/μm
Formulation 2	1816.67	449.07	871.67	169.75
Formulation 3	1831.43	448.23	950.00	352.37
Formulation 1	2258.33	502.41	983.33	331.16
ALG/Zn	1710.00	411.58	535.00	224.54

Table 3. ANOVA table between the groups and within the groups.

Source of Variation	Sum of Squares (SS)	Degrees of Freedom (DF)	Mean Square (MS)	F-Statistic	*p*-Value
Between Groups	996,497.10	3	332,165.70	7.91	<0.00001
Within Groups	1,007,658.09	24	41,986.59		
Total	2,004,155.19	27			

The provided tables present the means and variances for wet and dry formulations across Formulation 2, Formulation 3, Formulation 1, and ALG/Zn. The ANOVA results indicate significant differences among the group means, with an F-statistic of 7.91 and a *p*-value of < 0.0001. This suggests that the formulation type significantly affects the measured outcomes.

Surface elemental analysis by EDX revealed apparent differences in metal distribution among the formulations, providing insight into how AgNPs and ZnONPs interact with the alginate network during gelation and drying. The similar Zn surface content in ALG/Zn and Formulation 1 suggests that the presence of AgNPs does not strongly interfere with Zn^{2+} migration toward the bead surface, which is expected because divalent ions such as Zn^{2+} possess a high affinity for guluronic acid blocks and tend to accumulate near the outer gelation front during ionotropic crosslinking [10,30]. The markedly higher Zn content detected on the surfaces of Formulations 2 and 3 (8.25% and 6.05%, respectively) indicates that ZnO nanoparticles—unlike AgNPs—promote additional Zn enrichment near the surface, likely due to partial dissolution of ZnO in the slightly acidic alginate environment and subsequent binding of liberated Zn^{2+} at surface carboxylate sites, as previously demonstrated for ZnO–polysaccharide composites [31,32]. The absence of detectable Ag on the surfaces of Ag-loaded microparticles further supports the conclusion that AgNPs become more deeply embedded within the alginate matrix. This is consistent with studies showing that small AgNPs (typically <50 nm) rapidly diffuse toward the interior during gelation and become mechanically entrapped within the forming 3D network rather than adsorbing to the surface, especially when their surface charge is partially screened by the ionic crosslinking environment [33–35]. Moreover, alginate matrices form dense outer layers during Ca^{2+}/Zn^{2+}-driven gelation, which can restrict the outward migration of nanoparticles and favor their encapsulation within the interior [30]. Collectively, these findings align with previous reports showing preferential surface localization of metal ions with high alginate affinity (e.g., Zn^{2+}), in contrast to deeper incorporation of metallic nanoparticles that participate less directly in ionic crosslinking. The resulting metal distribution patterns are expected to influence antimicrobial performance and release behavior: Zn-rich surfaces typically support faster Zn^{2+} availability and immediate antimicrobial activity, whereas internalized AgNPs often provide slower, diffusion-controlled ion release over extended periods [32,34]. Thus, the EDX results in Figure 6 provide a mechanistic explanation for the distinct functional properties anticipated for each formulation.

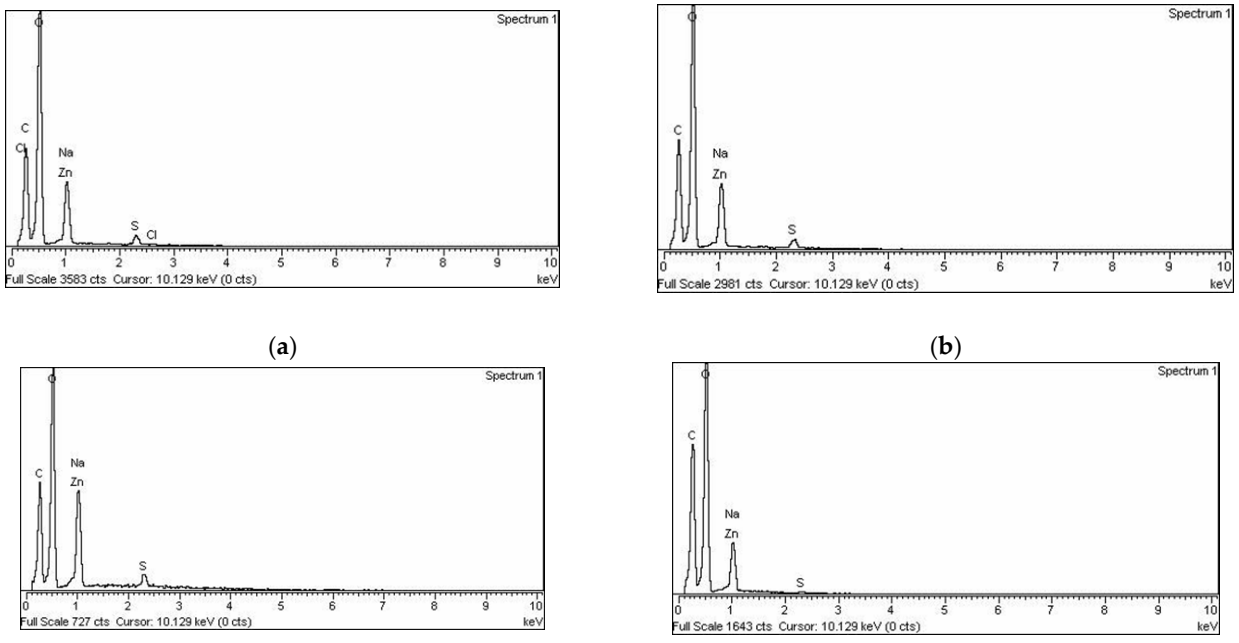

Figure 6. Surface elemental analysis using dispersive X-ray spectroscopy (EDX): ALG/Zn (**a**), Formulation 1, (**b**) Formulation 2 (**c**) and Formulation 3 (**d**).

3.3. In Vitro AgNP and ZnONP Release from Formulations

One of the most crucial properties of alginate microparticles is the ability to release encapsulated bioactive components over a specific time. The release of nanoparticles from alginate microparticles is influenced by the interplay of various factors, including the physical and chemical properties of the nanoparticles (size, surface properties, and charge), the structural and mechanical properties of alginate, the encapsulation method, and environmental conditions [24]. The swelling behavior of the microparticles reflected the influence of nanoparticle type on alginate network structure. Formulations containing AgNPs exhibited a higher degree of swelling than ALG/Zn, consistent with reports that negatively charged citrate-capped AgNPs can electrostatically repel alginate chains and reduce effective crosslinking, thereby increasing water uptake [27,33]. In contrast, ZnONP-loaded formulations showed markedly lower swelling, in agreement with previous studies demonstrating that Zn^{2+} and surface oxygen groups on ZnONPs enhance ionic interactions and hydrogen bonding with alginate, producing a denser, less permeable network [26,28]. This trend aligns with the literature describing reduced swelling in ZnO–alginate systems—often decreasing from >400% to ~100–400% upon ZnO incorporation—as Zn-mediated crosslinking restricts free volume and chain mobility [29]. The present results in Table 4 therefore align with established findings that AgNPs loosen alginate networks, whereas ZnONPs reinforce them, leading to distinct.

Table 4. Encapsulation efficiency (EE), loading capacity (LC), and degree of swelling (S_w) of microparticles.

Microparticles	EE/%	LC/mg g^{-1}	S_w/%
ALG/Zn			52.1 ± 0.7
Formulation 1	[a] 77.9 ± 1.37	[a] $1.9 \times 10^{-3} \pm 3.2 \times 10^{-5}$	63.8 ± 4.5
Formulation 2	[b] 98.6 ± 0.76	[b] $3.7 \times 10^{-5} \pm 7.6 \times 10^{-7}$	42.6 ± 2.9
Formulation 3	[a] 64.0 ± 2.51	[a] $1.5 \times 10^{-3} \pm 2.0 \times 10^{-5}$	42.5 ± 2.7
Formulation 3	[b] 98.9 ± 0.95	[b] $2.9 \times 10^{-5} \pm 0.5 \times 10^{-6}$	42.5 ± 2.7

[a] refers to AgNPs, and [b] refers to ZnONPs.

The trends in encapsulation efficiency (EE) and loading capacity (LC) observed in Table 2 highlight how nanoparticle concentration, surface chemistry, and alginate–ion interactions collectively determine nanoparticle retention during ionotropic gelation. The exceptionally high EE for ZnONPs (≈99%) despite their low initial loading (1%) is consistent with reports that Zn^{2+} released from partially ionized ZnO exhibits strong affinity for alginate carboxylate groups, promoting rapid coordination and highly effective entrapment within the forming gel network [26,28]. Similar near-quantitative retention of ZnO or Zn^{2+} species has been reported in Zn–alginate hydrogels and beads, where EE values commonly exceed 90–98% due to strong ionic crosslinking and limited nanoparticle mobility once gelation begins [31,32]. In contrast, the lower EE measured for AgNPs (≈79%), despite their higher input concentration (5%), aligns with earlier studies showing that citrate-capped AgNPs—being negatively charged and not participating directly in ionic crosslinking—are more prone to diffusion out of the bead before complete network formation, resulting in significantly reduced retention (typically 60–85%) compared to metal ions or oxide nanoparticles [33,34]. The even lower EE observed in the co-loaded formulations (≈64%) likely reflects competitive or altered Zn^{2+}-mediated crosslinking kinetics. Previous work demonstrates that the presence of multivalent ions can accelerate gel front formation, thereby decreasing the time window for nanoparticle entrapment and disproportionately reducing the retention of non-crosslinking nanoparticles such as AgNPs [10,30]. Similar reductions in EE for AgNPs in the presence of divalent ions (Ca^{2+}, Zn^{2+}, Ba^{2+}) have been reported, with decreases of up to 20–30% attributed to faster diffusion–reaction

fronts and steric or electrostatic exclusion effects during matrix formation [34]. Overall, the encapsulation behavior observed here is consistent with published findings and reinforces the mechanistic interpretation that ZnONPs—or Zn^{2+} released from them—integrate readily into the alginate network. In contrast, AgNP retention is primarily governed by physical trapping and, therefore, is more sensitive to gelation kinetics and competing ionic interactions.

The release of AgNPs and ZnONPs from the formulations dispersed in distilled water is shown in Figure 7. Results are presented as changes in the cumulative fraction of AgNPs or ZnONPs released over time. AgNP release profiles from Formulations 1 and 3 (Figure 7a) showed a rapid initial release followed by a slower release in accordance with a power law equation. Release profiles of ZnONPs from Formulations 2 and 3 showed several time-dependent release intervals. In the first interval (I), the profiles followed a power equation. The second intervals (II) were characterized by a linear dependence of release with time, and the third intervals (III) were characterized by a slowing down of release. Such release profiles imply a change in alginate mechanisms during the release process. To gain a deeper understanding of the release mechanism and kinetics of nanoparticles from microparticle formulations, two mathematical models—the power law model and zero-order kinetics [32]—were used to process the release data.

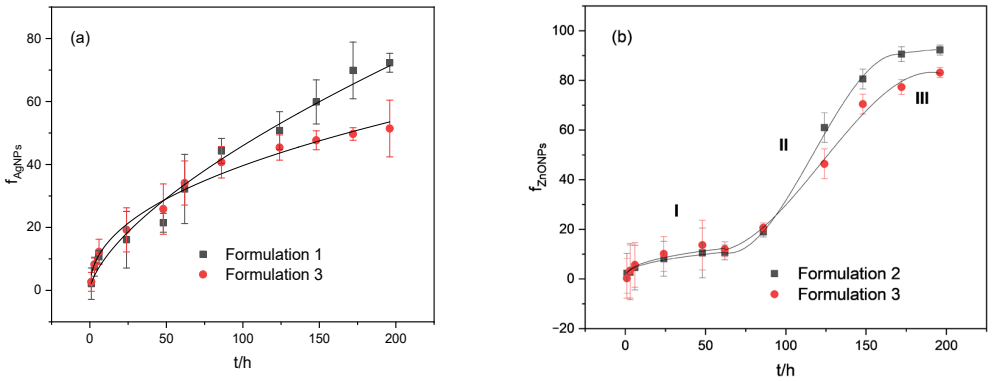

Figure 7. Fraction of released AgNPs (f_{AgNPs}) (**a**) and ZnNPs (f_{ZnNPs}) (**b**) from formulations with time (t). Error bars indicate the standard deviation of the means. Samples are denoted.

According to the power law empirical model [32], different controlling mechanisms may be distinguished by the following equation:

$$f = kt^n \quad (5)$$

where k is a release constant characteristic for a particular system considering structural and geometrical aspects, n is the release exponent representing the release mechanism ($n < 0$—Fickian diffusion, $n > 1$—polymer swelling and relaxation of the polymeric matrix—Type II transport, $0.43 < n < 1$—a combination of the two diffusion mechanisms and Type II transport (anomalous transport)), and t is the release time. Zero-order kinetics can be described with the following equation [34]:

$$A_t/A_o = K_0 t \quad (6)$$

where A_o is the initial amount of active agent loaded in the microparticle, A_t is the amount of active agent released during time t, K_0 is the proportionality constant, and t is the time.

The zero-order release rate constant indicates the amount of drug released per unit time, regardless of the concentration remaining in the matrix; the rate is independent of concentration. The zero order of fit, indicating a nearly constant release, makes the

formulations suitable for sustained-release systems [35]. The release kinetics parameters of Formulation 1, Formulation 2, and Formulation 3 in distilled water at 25 °C. are presented in Table 5.

Table 5. Release kinetics parameters of Formulation 1, Formulation 2, and Formulation 3 in distilled water at 25 °C. (I) Korsmeyer–Peppas model (k/h^n is a kinetic constant, and n is the release exponent), and (II) zero-order kinetics (K_o is the zero-order release rate constant). R^2 is a correlation coefficient.

Formulation		I			II	
		k/h^n	n	R^2	K_o/t	R^2
Formulation 1	f_{Ag}	2.26	0.65	0.98		
Formulation 3	f_{Ag}	5.01	0.45	0.99		
Formulation 2 (I)	f_{Zn}	2.39	0.36	0.99		
Formulation 2 (II)	f_{Zn}				1.00	0.99
Formulation 3 (I)	f_{Zn}	2.54	0.38	0.98		
Formulation 3 (II)	f_{Zn}				0.80	0.99

The exponent (n) between 1 and 0.43 indicates that the release rate of silver nanoparticles (AgNPs) from Formulations 1 and 3 is governed by a combination of diffusion and polymer swelling/relaxation [65]. This involves the diffusion of nanoparticles through the alginate matrix and the relaxation of polymer chains. Increased swelling relaxes alginate chains, loosening the network structure and reducing crosslinking density [66]. In Formulation 3, the presence of AgNPs and zinc oxide nanoparticles (ZnONPs) significantly alters the network structure. Smaller, spherical AgNPs diffuse more readily than larger, elongated ZnONPs, which have rough surfaces [67]. The release rate constant (k) indicates a faster release of AgNPs when co-loaded with ZnONPs, suggesting that strong ZnONP binding to the alginate matrix enhances AgNP release [68]. ZnONP release profiles from Formulations 2 and 3 demonstrate dynamic changes over time. Initially, they follow Fickian diffusion (with $n < 0.43$), as higher crosslinking density promotes ion diffusion [69]. In the second interval, ZnONPs are released at a constant rate, exhibiting zero-order kinetics. The constant (K) represents the release rate of ZnONPs, with a higher (K) indicating a faster release from Formulation 2 [70]. By the third interval, ZnONP release becomes erosion-controlled, dictated by matrix degradation.

4. Influence of Novel Formulations on Pythopatogenic Fungus *Fusarium solani*

4.1. Morphological Characterization of Fusarium solani

Figure 8 presents optical microscopy (OM) and scanning electron microscopy (SEM) microphotographs of *Fusarium solani*, revealing distinct structural features. The optical image of the hyphal tip region (Figure 8a) shows several apical hyphae/conidiophore-like projections, characterized by evident septa and cytoplasmic inclusions. The slender, filamentous hyphae originate from a single base, with individual hyphae measuring just a few micrometers in diameter. The septa, visible as transverse lines along the hyphae, confirm the presence of septate ascomycete or basidiomycete hyphae, distinguishing them from coenocytic forms [71].

The SEM microphotograph (Figure 8b) reveals hyphae with irregular surface contours, including constrictions, knobby swellings, and areas of collapse or wrinkling. These surface irregularities suggest mechanical stress and dehydration during sample preparation, a finding echoed by other researchers [72]. The absence of a smooth, continuous extracellular matrix layer at this resolution suggests a complex cell wall architecture, potentially comprising chitin microfibrils embedded in a glucan matrix or surface-bound materials [73].

Energy-dispersive spectroscopy (EDS) analysis indicates that the major elements on the hyphal surface are carbon and oxygen, followed by nitrogen, sodium, magnesium, and potassium. This elemental composition aligns with earlier studies indicating that fungal cell walls are rich in polysaccharides, particularly chitin and glucans, which play crucial roles in maintaining structural integrity and protecting against environmental stress [71]. A comparative analysis with other authors' findings reveals consistency in the morphological characteristics of *Fusarium solani*. For instance, similar surface irregularities and elemental compositions have been documented, reinforcing the idea that these structural features indicate the species' adaptability to environmental conditions [54]. Overall, these observations provide insight into the physiological state of *Fusarium solani*, underscoring its structural complexity and ecological adaptability.

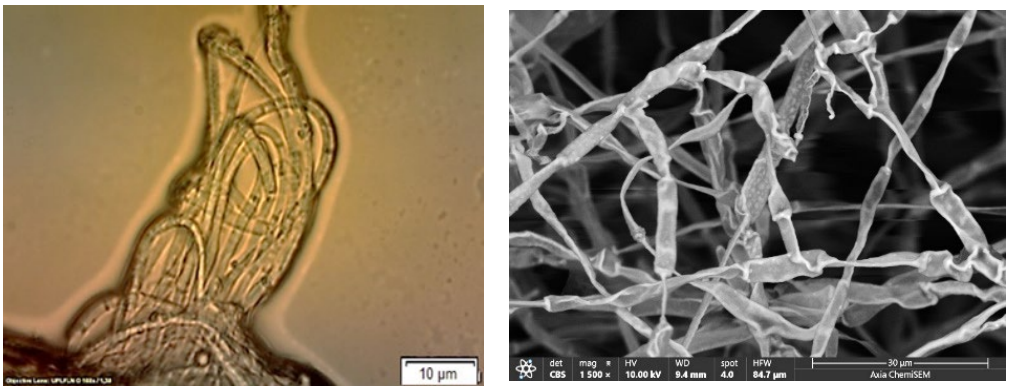

(**a**) (**b**)

Figure 8. OM (**a**) and SEM (**b**) microphotographs of *Fusarium solani*. The scale bars are indicated.

4.2. Influence of Formulations on the Fusarium solani Hyphae

The effects of novel formulations on *Fusarium solani* hyphae are presented in Figure 9. The control system shows typical tubular hyphae with regular septation (Figure 9a). ALG/Zn addition causes mild reduction in hyphal density with localized buckling/swelling (Figure 9b), while Formulation 1 results in marked deformation, wall corrugation, and focal lysis (Figure 9c), Formulation 2 leads to fragmented networks and granular debris consistent with ROS damage (Figure 9d), and Formulation 3 causes severe collapse and clumping, indicating additive/synergistic injury (Figure 9e). The control sample exhibits typical tubular hyphae with regular septation, characterized by smooth walls and high density (Figure 9a). The addition of ALG/Zn results in a mild reduction in hyphal density and localized buckling, indicative of Zn^{2+} stress on cell wall synthesis and membrane function [72] (Figure 9b).

Formulation 1 induces marked deformation, with irregular thickness and surface corrugation, as well as focal lysis of hyphae (Figure 9c). These changes suggest severe membrane degradation, consistent with findings that highlight the impact of environmental stressors on fungal integrity [74].

Formulation 2 presents disrupted networks with fragmented filaments and granular debris, a pattern aligning with ROS-mediated damage typically associated with ZnO nanoparticles (Figure 9d) [75]. Formulation 3 shows the most dramatic effect—densely corrugated, clumped, and severely deformed hyphae with widespread collapse and loss of continuity. This visual phenotype indicates additive/synergistic injury to the wall and membrane, consistent with simultaneous Ag- and ZnO-driven stress. Overall, the inhibition trend from the micrographs is as follows:

Control < ALG/Zn < Formulation 1 ≈ Formulation 2 < Formulation 3 (the strongest).

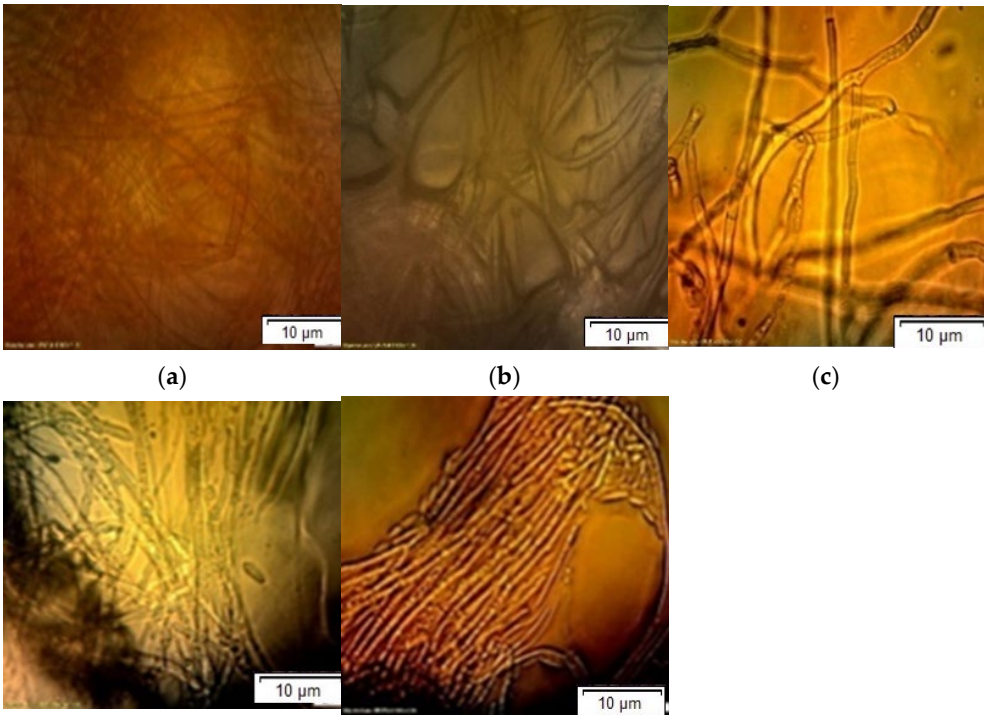

Figure 9. Optical micrographs showing the effect of microparticle formulations on *Fusarium solani* hyphae. (**a**) Control: normal tubular hyphae with regular septation. (**b**) ALG/Zn: mild reduction in hyphal density with localized buckling/swelling. (**c**) Formulation 1: marked deformation, wall corrugation, and focal lysis. (**d**) Formulation 2: fragmented networks and granular debris consistent with ROS damage. (**e**) Formulation 3: severe collapse and clumping, indicating additive/synergistic injury. Scale bars are shown in each micrograph.

Morphological changes indicate that Formulation 3 is most promising for applications requiring rapid protection against Fusarium species, while Formulations 1 and 2 still show strong effects and may be selected based on regulatory or cost constraints.

4.3. FTIR Spectrum of Fusarium solani After the Application of Formulations

The changes in the FTIR spectrum of the phytopathogenic fungi *Fusarium solani* after the application of microparticle formulations are presented in Figure 10. When compared to the untreated control, the FTIR spectra of *Fusarium solani* treated with formulations consistently show changes. The aliphatic C–H stretching bands (2920/2850 cm^{-1}) show modifications suggestive of changed lipid order, while the wide O–H/N–H stretching band (3600–3100 cm^{-1}) loses intensity [23]. Notably, Formulations 2 and 3 show an increase in the intensity of the carbonyl band around 1740 cm^{-1}, which indicates lipid peroxidation [76,77]. The broadening and shifting of the amide I and II regions (1700–1500 cm^{-1}) suggest a change in protein structure and most likely metal coordination to peptide/carboxyl groups [78]. Lastly, there is a noticeable decrease in intensity in the carbohydrate fingerprint region (1200–900 cm^{-1}), which is consistent with disruption of cell wall polysaccharides (chitin/β-glucans) [79]. The effects are most noticeable for Formulations 2 and 3. These spectral changes, along with microscopy and viability tests (Figures 9 and 10), support a multimodal antifungal mechanism involving ROS generation, membrane destabilization, and direct binding of metal ions to cell wall and protein functional groups [80,81].

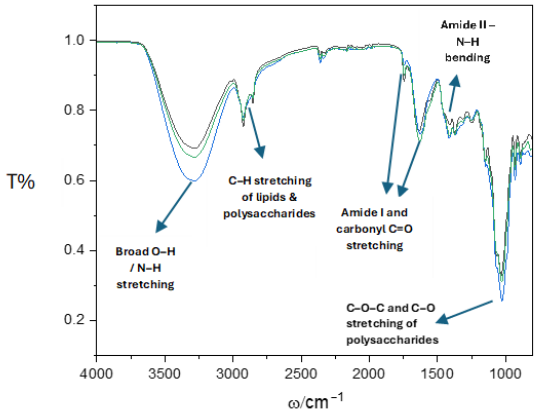

Figure 10. FTIR spectrum of *Fusarium solani* (black line), *Fusarium solani* treated with Formulation 1, Formulation 2 (blue line), and Formulation 3 (green line).

4.4. Antifungal Effect of Formulations on Fusarium solani

Microphotographs of plates inoculated with F. solani and treated with different microparticle formulations show antifungal activity (Figure 11). Comparison of control and treated samples demonstrates the effectiveness of the novel formulations. The control plates exhibit typical *F. solani* growth characteristics, including thick, fluffy mycelial growth and sporulation. Treatment with Formulation 1 resulted in reduced mycelial growth (Figure 11a). The mean inhibition was 80.7 ± 1.4%, which was significantly greater than that of the control (ANOVA, $p < 0.05$). Treatment with Formulation 2 (Figure 11b) exhibited much less fungal growth than the control, with a mean inhibition of 91.4 ± 1.1% ($p < 0.05$). Treatment with Formulation 3 (Figure 11c) showed a dramatic reduction in fungal growth, with complete inhibition (99.7 ± 0.5%), significantly higher than both the F1 and F2 groups (Tukey test, $p < 0.05$). These results confirm that AgNPs, ZnONPs, and their combination exhibit potent antifungal activity. Their known mechanisms (including membrane disruption, ROS generation, and synergistic interaction) likely contributed to the observed inhibition. All tested treatments may be useful methods for managing phytopathogenic fungi in agricultural settings [78,80,82–84].

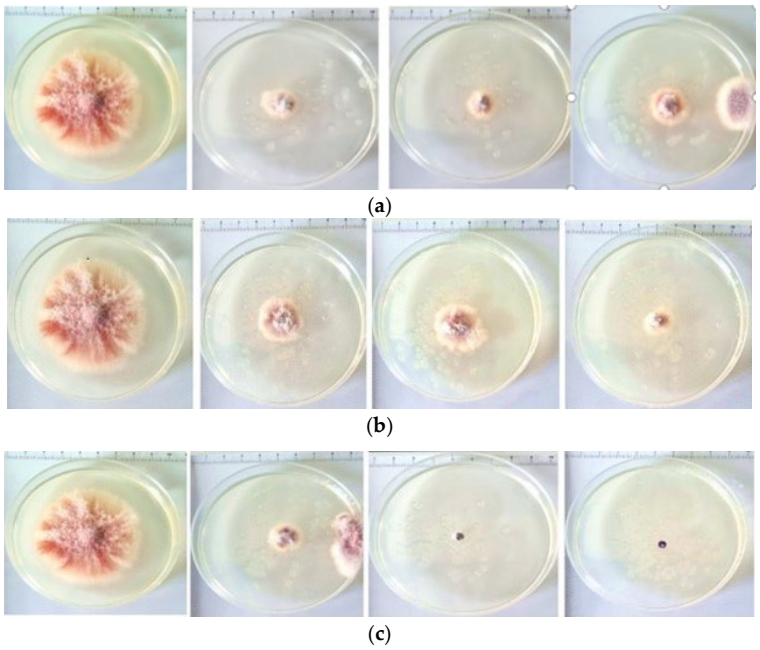

Figure 11. Antifungal activity of Formulation 1 (**a**), Formulation 2 (**b**), and Formulation 3 (**c**) on phytopathogenic *Fusarium solani*.

5. Conclusions

This study introduces a scientifically novel, zinc-crosslinked alginate microparticle platform capable of co-delivering AgNPs and ZnONPs with tunable structural and release properties that significantly enhance antifungal performance. By systematically comparing single- and dual-nanoparticle formulations, we demonstrate that AgNPs and ZnONPs exert opposing yet complementary effects on the alginate network: AgNPs reduce crosslinking density, producing rough and highly porous particles, whereas ZnONPs strengthen hydrogen bonding and ionic coordination, yielding smoother particles with smaller pores. Co-loaded formulations integrate these contrasting behaviors to achieve a balanced structure optimized for sustained release. Quantitative analysis confirms the distinct transport behaviors of each nanoparticle type. AgNP release followed anomalous diffusion (n = 0.65), while ZnONP release shifted from Fickian diffusion ($n \approx$ 0.36–0.38) to zero-order kinetics (K_0 = 1.00 for ZnONPs alone; 0.80 for co-loaded particles), demonstrating improved release uniformity and prolonged availability. Encapsulation efficiencies remained high across formulations, reaching 77.9% for AgNPs and 98.6% for ZnONPs, with co-loaded systems maintaining 64.0% and 98.9%, respectively. The antifungal efficacy achieved in this study represents a substantial advancement over classical single-agent approaches. AgNP-loaded and ZnONP-loaded particles inhibited *Fusarium solani* by 80.7% and 91.4%, respectively, while co-loaded microparticles produced near-complete inhibition (99.7%), confirming additive-to-synergistic effects. Microscopic evaluation further revealed severe hyphal deformation, fragmentation, and ROS-mediated damage uniquely intensified in the dual-nanoparticle system. Overall, this work provides the first integrated mechanistic and quantitative demonstration that co-loading AgNPs and ZnONPs in zinc-crosslinked alginate microparticles yields a synergistic, sustained-release antifungal platform. These findings establish a foundation for designing next-generation nanoparticle delivery systems for crop protection. Future work should extend evaluation to multiple phytopathogens, in planta studies, and environmental safety assessments to support practical deployment.

Author Contributions: M.V.: Writing—original draft; I.R.M.: Writing—review & editing; L.S.: Formal analysis, Project administration; J.K.: Data curation; I.K.: Validation; S.Š.: Data curation; M.M. (Marijan Marciuš): Methodology; M.M. (Mislav Majdak): Resources; N.J.: Investigation, Visualization; L.Ž.G.: Investigation; I.Š.: Formal analysis; K.M.: Conceptualization. All authors have read and agreed to the published version of the manuscript.

Funding: This research was funded by the Croatian Science Foundation grant number IP-2019-04-1381 (project under the title "Antibacterial coating for biodegradable medicine materials ABBAMEDICA"). Any opinions, findings, and conclusions or recommendations expressed in this material are those of the authors and do not necessarily reflect the views of the Croatian Science Foundation.

Institutional Review Board Statement: Not applicable.

Informed Consent Statement: Not applicable.

Data Availability Statement: The original contributions presented in this study are included in the article. Further inquiries can be directed to the corresponding author.

Conflicts of Interest: The authors declare no conflicts of interest. The funders had no role in the design of the study; in the collection, analyses, or interpretation of data; in the writing of the manuscript; or in the decision to publish the results.

References

1. Islam, T.; Danishuddin; Tamanna, N.T.; Matin, M.N.; Barai, H.R.; Haque, M.A. Resistance Mechanisms of Plant Pathogenic Fungi to Fungicide, Environmental Impacts of Fungicides, and Sustainable Solutions. *Plants* **2024**, *13*, 2737. [CrossRef]
2. Fisher, M.C.; Gurr, S.J.; Cuomo, C.A.; Blehert, D.S.; Jin, H.; Stukenbrock, E.H.; Stajich, J.E.; Kahmann, R.; Boone, C.; Denning, D.W.; et al. Threats Posed by the Fungal Kingdom to Humans, Wildlife, and Agriculture. *mBio* **2020**, *11*, e00449-20. [CrossRef] [PubMed]
3. Dakal, T.C.; Kumar, A.M.; Majumdar, R.S.; Yadav, V. Mechanistic Basis of Antimicrobial Actions of Silver Nanoparticles. *Front. Microbiol.* **2016**, *7*, 1831. [CrossRef] [PubMed]
4. Yagoub, A.E.A.; Al-Shammari, G.M.; Al-Harbi, L.N.; Subash-Babu, P.; Elsayim, R.; Mohammed, M.A.; Yahya, M.A.; Fattiny, S.Z.A. Antimicrobial Properties of Zinc Oxide Nanoparticles Synthesized from *Lavandula pubescens* Shoot Methanol Extract. *Appl. Sci.* **2022**, *12*, 11613. [CrossRef]
5. Canaparo, R.; Foglietta, F.; Limongi, T.; Serpe, L. Biomedical Applications of Reactive Oxygen Species Generation by Metal Nanoparticles. *Materials* **2021**, *14*, 53. [CrossRef]
6. Azam, A.; Ahmed, A.S.; Oves, M.; Khan, M.S.; Habib, S.S.; Memic, A. Antimicrobial activity of metal oxide nanoparticles against Gram-positive and Gram-negative bacteria: A comparative study. *Int. J. Nanomed.* **2012**, *7*, 6003–6009. [CrossRef]
7. Pelgrift, R.Y.; Friedman, A.J. Nanotechnology as a therapeutic tool to combat microbial resistance. *Adv. Drug Deliv. Rev.* **2013**, *65*, 1803–1815. [CrossRef]
8. Harun-Ur-Rashid, M.; Foyez, T.; Krishna, S.B.N.; Podal, S.; Imran, A.B. Recent advances of silver nanoparticle—Based polymer nanocomposites for biomedical applications. *RSC Adv.* **2025**, *15*, 8480–8505. [CrossRef]
9. Muzammil, S.; Ashraf, A.; Siddique, M.H.; Aslam, B.; Rasul, I.; Abbas, R.; Afzal, M.; Faisal, M.; Hayat, S. A review on toxicity of nanomaterials in agriculture: Current scenario and future prospects. *Sci. Prog.* **2023**, *106*, 368504231221672. [CrossRef]
10. Lee, K.Y.; Mooney, D.J. Alginate: Properties and biomedical applications. *Prog. Polym. Sci.* **2012**, *37*, 106–126. [CrossRef]
11. Augst, A.D.; Kong, H.J.; Mooney, D.J. Alginate hydrogels as biomaterials. *Macromol. Biosci.* **2006**, *6*, 623–633. [CrossRef] [PubMed]
12. Malektaj, H.; Drozdov, A.D.; deClaville Christiansen, J. Mechanical Properties of Alginate Hydrogels Cross-Linked with Multivalent Cations. *Polymers* **2023**, *15*, 3012. [CrossRef] [PubMed]
13. Guo, L.; Zheng, D.; Xu, J.; Gao, X.; Fu, X.; Zhang, Q. Effects of ionic crosslinking on physical and mechanical properties of alginate mulching films. *Carbohydr. Polym.* **2016**, *136*, 259–265. [CrossRef] [PubMed]
14. Fleten, K.G.; Hyldbakk, A.; Einen, C.; Benjakul, S.; Strand, B.L.; Davies, C.D.L.; Mørch, Ý.; Flatmark, K. Alginate Microsphere Encapsulation of Drug-Loaded Nanoparticles: A Novel Strategy for Intraperitoneal Drug Delivery. *Mar. Drugs* **2022**, *20*, 744. [CrossRef]
15. Abubakr, N.; Lin, S.X.; Chen, X.D. Effects of Drying Methods on the Release Kinetics of Vitamin B_{12} in Calcium Alginate Beads. *Dry. Technol.* **2009**, *27*, 1258–1265. [CrossRef]
16. Natori, N.; Shibano, Y.; Hiroki, A.; Taguchi, M.; Miyajima, A.; Yoshizawa, K.; Kawano, Y.; Hanawa, T. Preparation and Evaluation of Hydrogel Film Containing Tramadol for Reduction of Peripheral Neuropathic Pain. *J. Pharm. Sci.* **2023**, *112*, 132–137. [CrossRef]
17. Chandran, S.P.; Chaudhary, M.; Pasricha, R.; Ahmad, A.; Sastry, M. Synthesis of gold nanotriangles and silver nanoparticles using *Aloevera* plant extract. *Biotechnol. Prog.* **2006**, *22*, 577–583. [CrossRef]
18. Elumalai, E.K.; Prasad, T.N.V.K.V.; Hemachandran, J.; Therasa, S.V.; Thirumalai, T.; David, E.J. Extracellular synthesis of silver nanoparticles using leaves of *Euphorbia hirta* and their antibacterial activities. *J. Pharm. Sci. Res.* **2010**, *2*, 549–554. Available online: https://europub.co.uk/articles/-A-85195 (accessed on 11 July 2025).
19. Vanaja, M.; Annadurai, G. *Coleus aromaticus* leaf extract mediated synthesis of silver nanoparticles and its bactericidal activity. *Appl. Nanosci.* **2013**, *3*, 217–223. [CrossRef]
20. Wojnarowicz, J.; Opalinska, A.; Chudoba, T.; Gierlotka, S.; Mukhovskyi, R.; Pietrzykowska, E.; Sobczak, K.; Lojkowski, W. Effect of Water Content in Ethylene Glycol Solvent on the Size of ZnO Nanoparticles Prepared Using Microwave Solvothermal Synthesis. *J. Nanomater.* **2016**, *2016*, 2789871. [CrossRef]
21. Zhang, L.; Jiang, Y.; Ding, Y.; Daskalakis, N.; Jeuken, L.; Povey, M.; O'Neill, A.J.; York, D.W. Mechanistic investigation into antibacterial behaviour of suspensions of ZnO nanoparticles against *E. coli*. *J. Nanoparticle Res.* **2010**, *12*, 1625–1636. [CrossRef]
22. Sun, R.; Xia, Q. Release mechanism of lipid nanoparticles immobilized within alginate beads influenced by nanoparticle size and alginate concentration. *Colloid Polym. Sci.* **2019**, *297*, 1183–1198. [CrossRef]
23. Vinceković, M.; Jurić, S.; Vlahoviček-Kahlina, K.; Martinko, K.; Šegota, S.; Marijan, M.; Krčelić, A.; Svečnjak, L.; Majdak, M.; Nemet, I.; et al. Novel Zinc/Silver Ions-Loaded Alginate/Chitosan Microparticles Antifungal Activity against *Botrytis cinerea*. *Polymers* **2023**, *15*, 4359. [CrossRef] [PubMed]
24. Jay, S.M.; Saltzman, W.M. Controlled delivery of VEGF via modulation of alginate microparticle ionic crosslinking. *J. Control. Release* **2009**, *134*, 26–34. [CrossRef] [PubMed]
25. Siepmann, J.; Siepmann, F. Modeling of diffusion controlled drug delivery. *J. Control. Release* **2012**, *161*, 351–362. [CrossRef]

26. Khvorostina, M.A.; Algebraistova, P.Y.; Nedorubova, I.A.; Bukharova, T.B.; Goldshtein, D.V.; Teterina, A.Y.; Komlev, V.S.; Popov, V.K. The Influence of Crosslinking Agents on the Matrix Properties of Hydrogel Structures Based on Sodium Alginate. *Inorg. Mater. Appl. Res.* **2024**, *15*, 388–394. [CrossRef]
27. Peretiatko, C.D.S.; Hupalo, E.A.; da Rocha Campos, J.R.; Budziak Parabocz, C.R. Efficiency of Zinc and Calcium Ion Crosslinking in Alginate-coated Nitrogen Fertilizer. *Orbital Electron. J. Chem.* **2018**, *10*, 218–225. [CrossRef]
28. Boughbina-Portolés, A.; Sanjuan-Navarro, L.; Moliner-Martínez, Y.; Campíns-Falcó, P. Study of the Stability of Citrate Capped AgNPs in Several Environmental Water Matrices by Asymmetrical Flow Field Flow Fractionation. *Nanomaterials* **2021**, *11*, 926. [CrossRef]
29. Rokstad, A.M.A.; Lacik, I.; de Vos, P.; Strand, B.L. Advances in biocompatibility and physico-chemical characterization of microspheres for cell encapsulation. *Adv. Drug Deliv. Rev.* **2014**, *67–68*, 111–130. [CrossRef]
30. Cleetus, C.M.; Alvarez Primo, F.; Fregoso, G.; Lalitha Raveendran, N.; Noveron, J.C.; Spencer, C.T.; Ramana, C.V.; Joddar, B. Alginate Hydrogels with Embedded ZnO Nanoparticles for Wound Healing Therapy. *Int. J. Nanomed.* **2020**, *15*, 5097–5111. [CrossRef]
31. Ingar Draget, K.; Østgaard, K.; Smidsrød, O. Homogeneous alginate gels: A technical approach. *Carbohydr. Polym.* **1990**, *14*, 159–178. [CrossRef]
32. Bruschi, M.L. Mathematical models of drug release. In *Strategies to Modify the Drug Release from Pharmaceutical Systems*; Bruschi, M.L., Ed.; Woodhead Publishing: Sawston, UK, 2015; pp. 63–86. [CrossRef]
33. Lao, L.L.; Peppas, N.A.; Boey, F.Y.-C.; Venkatraman, S.S. Modeling of Drug Release from Bulk-Degrading Polymers. *Int. J. Pharm.* **2011**, *418*, 28–41. [CrossRef] [PubMed]
34. Azadi, S.; Ashrafi, H.; Azadi, A. Mathematical modeling of drug release from swellable polymeric nanoparticles. *J. Appl. Pharm. Sci.* **2017**, *7*, 125–133. Available online: http://creativecommons.org/licenses/by-nc-sa/3.0/ (accessed on 17 August 2025).
35. Laracuente, M.L.; Yu, M.H.; McHugh, K.J. Zero-order drug delivery: State of the art and future prospects. *J. Control. Release* **2020**, *327*, 834–856. [CrossRef]
36. Parvin, N.; Joo, S.W.; Mandal, T.K. Nanomaterial-Based Strategies to Combat Antibiotic Resistance: Mechanisms and Applications. *Antibiotics* **2025**, *14*, 207. [CrossRef]
37. Al-Gaashani, R.; Pasha, M.; Jabbar, K.A.; Shetty, A.R.; Bagiah, H.; Mansour, S.; Kochkodan, V.; Lawler, J. Antimicrobial activity of ZnO-Ag-MWCNTs nanocomposites prepared by a simple impregnation–calcination method. *Sci. Rep.* **2023**, *13*, 21418. [CrossRef]
38. AlQurashi, D.M.; AlQurashi, T.F.; Alam, R.I.; Shaikh, S.; Tarkistani, M.A.M. Advanced Nanoparticles in Combating Antibiotic Resistance: Current Innovations and Future Directions. *J. Nanotheranostics* **2025**, *6*, 9. [CrossRef]
39. Dube, E.; Okuthe, G.E. Silver Nanoparticle-Based Antimicrobial Coatings: Sustainable Strategies for Microbial Contamination Control. *Microbiol. Res.* **2025**, *16*, 110. [CrossRef]
40. Sirelkhatim, A.; Mahmud, S.; Seeni, A.; Kaus, N.H.M.; Ann, L.C.; Bakhori, S.K.M.; Hasan, H.; Mohamad, D. Review on Zinc Oxide Nanoparticles: Antibacterial Activity and Toxicity Mechanism. *Nano-Micro Lett.* **2015**, *7*, 219–242. [CrossRef]
41. Gautam, S.; Das, D.K.; Kaur, J.; Kumar, A.; Ubaidullah, M.; Hasan, M.; Yadav, K.K.; Gupta, R.K. Transition metal-based nanoparticles as potential antimicrobial agents: Recent advancements, mechanistic, challenges, and future prospects. *Discov. Nano* **2023**, *18*, 84. [CrossRef]
42. Zeng, Z.; Patel, J.; Lee, S.-H.; McCallum, M.; Tyagi, A.; Yan, M.; Shea, K.J. Synthetic polymer nanoparticle–polysaccharide interactions: A systematic study. *J. Am. Chem. Soc.* **2012**, *134*, 2681–2690. [CrossRef] [PubMed]
43. Scholtz, L.; Tavernaro, I.; Eckert, J.G.; Lutowski, M.; Geiβler, D.; Hertwig, A.; Hidde, G.; Bigall, N.C.; Resch-Genger, U. Influence of nanoparticle encapsulation and encoding on the surface chemistry of polymer carrier beads. *Sci. Rep.* **2023**, *13*, 11957. [CrossRef] [PubMed]
44. Cheng, X.; Xie, Q.; Sun, Y. Advances in nanomaterial-based targeted drug delivery systems. *Front. Bioeng. Biotechnol.* **2023**, *11*, 1177151. [CrossRef] [PubMed]
45. Singireddy, A.R.; Pedireddi, S.R. Advances in lopinavir formulations: Strategies to overcome solubility, bioavailability, and stability challenges. *Prospect. Pharm. Sci.* **2024**, *22*, 105–121. [CrossRef]
46. Coates, J. Interpretation of Infrared Spectra: A Practical Approach. In *Encyclopedia of Analytical Chemistry*; Meyers, R.A., Ed.; John Wiley & Sons Ltd.: Chichester, UK, 2000; pp. 10881–10882.
47. Goldstein, J.I.; Newbury, D.E.; Echlin, P.; Joy, D.C.; Romig, A.D.; Lyman, C.E.; Fiori, C.; Lifshin, E. *Scanning Electron Microscopy and X-Ray Microanalysis: A Text for Biologists, Materials Scientists, and Geologists*, 2nd ed.; Springer: New York, NY, USA, 1992. [CrossRef]
48. Wang, C.; Gao, X.; Chen, Z.; Chen, Y.; Chen, H. Preparation, Characterization and Application of Polysaccharide-Based Metallic Nanoparticles: A Review. *Polymers* **2017**, *9*, 689. [CrossRef]
49. Zhang, N.; O'Donnell, K.; Sutton, D.A.; Nalim, F.A.; Summerbell, R.C.; Padhye, A.A.; Geiser, D.M. Members of the *Fusarium solani* Species Complex That Cause Infections in Both Humans and Plants Are Common in the Environment. *J. Clin. Microbiol.* **2006**, *44*, 2186–2190. [CrossRef]

50. Leslie, J.F.; Summerell, B.A. *The Fusarium Laboratory Manual*; Blackwell Publishing: Hoboken, NJ, USA, 2006; pp. 1–2. [CrossRef]
51. Vinceković, M.; Jalšenjak, N.; Topolovec-Pintarić, S.; Đermić, E.; Bujan, M.; Jurić, S. Encapsulation of Biological and Chemical Agents for Plant Nutrition and Protection: Chitosan/Alginate Microcapsules Loaded with Copper Cations and *Trichoderma viride*. *J. Agric. Food Chem.* **2016**, *64*, 8073–8083. [CrossRef]
52. Mokale, V.; Jitendra, N.; Yogesh, S.; Gokul, K. Chitosan reinforced alginate controlled release beads of losartan potassium: Design, formulation and in vitro evaluation. *J. Pharm. Investig.* **2014**, *44*, 243–252. [CrossRef]
53. Ouda, S.M. Antifungal Activity of Silver and Copper Nanoparticles on Two Plant Pathogens, *Alternaria alternata* and *Botrytis cinerea*. *Res. J. Microbiol.* **2014**, *9*, 34–42. Available online: https://scialert.net/abstract/?doi=jm.2014.34.42 (accessed on 10 July 2025). [CrossRef]
54. Martinko, K.; Ivanković, S.; Đermić, E.; Đermić, D. In vitro antifungal effect of phenylboronic and boric acid on *Alternaria alternata*. *Arch. Ind. Hyg. Toxicol.* **2022**, *73*, 83–87. [CrossRef]
55. Xue, W.M.; Yu, W.T.; Liu, X.D.; He, X.; Wang, W.X.; Ma, J. Chemical method of breaking the cell-loaded sodium alginate/chitosan microcapsules. *Chem. J. Chin. Univ.-Chin.* **2004**, *25*, 1342–1346. Available online: http://www.cjcu.jlu.edu.cn/EN/Y2004/V25/I7/1342 (accessed on 5 July 2025).
56. Zhang, X.F.; Liu, Z.G.; Shen, W.; Gurunathan, S. Silver Nanoparticles: Synthesis, Characterization, Properties, Applications, and Therapeutic Approaches. *Int. J. Mol. Sci.* **2016**, *17*, 1534. [CrossRef] [PubMed]
57. Murthy, K.R.S.; Raghu, G.K.; Binnal, P. Zinc Oxide Nanostructured Material for Sensor Application. *J. Biotechnol. Bioeng.* **2021**, *5*, 25–29. [CrossRef]
58. Bashir, S.; Awan, M.S.; Farrukh, M.A.; Naidu, R.; Khan, S.A.; Rafique, N.; Ali, S.; Hayat, I.; Hussain, I.; Khan, M.Z. In-vivo (*Albino Mice*) and in-vitro Assimilation and Toxicity of Zinc Oxide Nanoparticles in Food Materials. *Int. J. Nanomed.* **2022**, *17*, 4073–4085. [CrossRef] [PubMed]
59. Hussain, M.; Ansari, M.A.; Mir, F.A. Preparation, characterization and cooling performance of ZnO based Nanofluids. *Discov. Appl. Sci.* **2024**, *6*, 92. [CrossRef]
60. Swain, M.; Mishra, D.; Sahoo, G. A review on green synthesis of ZnO nanoparticles. *Discov. Appl. Sci.* **2025**, *7*, 997. [CrossRef]
61. Raut, N.S.; Deshmukh, P.R.; Umekar, M.J.; Kotagale, N.R. Zinc cross-linked hydroxamated alginates for pulsed drug release. *Int. J. Pharm. Investig.* **2013**, *3*, 194–202. [CrossRef]
62. Reig-Vano, B.; Huck-Iriart, C.; de la Flor, S.; Trojanowska, A.; Tylkowski, B.; Giamberini, M. Structural and mechanical analysis on mannuronate-rich alginate gels and xerogels beads based on Calcium, Copper and Zinc as crosslinkers. *Int. J. Biol. Macromol.* **2023**, *246*, 125659. [CrossRef]
63. Alzoubi, F.Y.; Al-zou'by, J.; Theban, S.K.; Alqadi, M.K.; Al-Khateeb, H.M.; AlSharo, E.S. Size, stability, and aggregation of citrates-coated silver nanoparticles: Contribution of background electrolytes. *Nanotechnol. Environ. Eng.* **2021**, *6*, 69. [CrossRef]
64. Azizi, S.; Shahri, M.M.; Mohamad, R. Green Synthesis of Zinc Oxide Nanoparticles for Enhanced Adsorption of Lead Ions from Aqueous Solutions: Equilibrium, Kinetic and Thermodynamic Studies. *Molecules* **2017**, *22*, 831. [CrossRef]
65. Popescu, I.; Constantin, M.; Solcan, G.; Ichim, D.L.; Rata, D.M.; Horodincu, L.; Solcan, C. Composite Hydrogels with Embedded Silver Nanoparticles and Ibuprofen as Wound Dressing. *Gels* **2023**, *9*, 654. [CrossRef] [PubMed]
66. Rizwan, M.; Yahya, R.; Hassan, A.; Yar, M.; Azzahari, A.D.; Selvanathan, V.; Sonsudin, F.; Abouloula, C.N. pH Sensitive Hydrogels in Drug Delivery: Brief History, Properties, Swelling, and Release Mechanism, Material Selection and Applica-tions. *Polymers* **2017**, *9*, 137, Erratum in *Polymers* **2017**, *9*, E225. https://Doi.Org/10.3390/Polym9060225. [CrossRef] [PubMed]
67. Cai, L.H.; Panyukov, S.; Rubinstein, M. Hopping Diffusion of Nanoparticles in Polymer Matrices. *Macromolecules* **2015**, *48*, 847–862. [CrossRef] [PubMed]
68. Toledo e Silva, S.H.; Bierhalz, A.C.K.; Moraes, Â.M. Influence of Nanoparticle Content and Cross-Linking Degree on Functional Attributes of Calcium Alginate-ZnO Nanocomposite Wound Dressings. *Membranes* **2025**, *15*, 108. [CrossRef]
69. Fu, Y.; Kao, W.J. Drug release kinetics and transport mechanisms of non-degradable and degradable polymeric deliv-ery systems. *Expert Opin. Drug Deliv.* **2010**, *7*, 429–444. [CrossRef]
70. Umar, W.; Czinkota, I.; Gulyás, M.; Aziz, T.; Hameed, M.K. Development and characterization of slow re-lease N and Zn fertilizer by coating urea with Zn fortified nano-bentonite and ZnO NPs using various binders. *Environ. Technol. Innov.* **2022**, *26*, 102250. [CrossRef]
71. Chehri, K.; Salleh, B.; Zakaria, L. Morphological and phylogenetic analysis of *Fusarium solani* species complex in Malaysia. *Microb. Ecol.* **2015**, *69*, 457–471. [CrossRef]
72. Torres-Rodriguez, J.A.; Reyes-Perez, J.J.; Carranza-Patino, M.S.; Herrera-Feijoo, R.J.; Preciado- Rangel, P.; Hernandez-Montiel, L.G. Biocontrol of *Fusarium solani*: Antifungal Activity of Chitosan and Induction of Defence Enzymes. *Plants* **2025**, *14*, 431. [CrossRef]
73. Gow, N.A.R.; Latge, J.P.; Munro, C.A. The Fungal Cell Wall: Structure, Biosynthesis, and Function. *Microbiol Spectr.* **2017**, *5*, 28513415. [CrossRef]
74. Yang, F.; Wang, L.; Li, S.; Yan, F.; Liang, W.; Yang, Q. Zinc exerts antifungal activity against *Fusarium pseudograminearum* by interfering with ROS accumulation regulated by transcription factor FpYap1. *Pest Manag. Sci.* **2025**, *81*, 8179–8190. [CrossRef]

75. Akpinar, I.; Unal, M.; Sar, T. Potential antifungal effects of silver nanoparticles (AgNPs) of different sizes against phytopathogenic *Fusarium oxysporum* f. sp. *radicis-lycopersici* (FORL) strains. *SN Appl. Sci.* **2021**, *3*, 506. [CrossRef]
76. Pielesz, A.; Biniaś, D.; Waksmańska, W.; Bobiński, R. Lipid bands of approx. 1740 cm^{-1} as spectral biomarkers and image of tissue oxidative stress. *Spectrochim. Acta Part A Mol. Biomol. Spectrosc.* **2023**, *286*, 121926. [CrossRef] [PubMed]
77. Moreno-Vargas, J.M.; Echeverry-Cardona, L.M.; Moreno-Montoya, L.E.; Restrepo-Parra, E. Evaluation of Antifungal Activity of Ag Nanoparticles Synthetized by Green Chemistry against *Fusarium solani* and *Rhizopus stolonifera*. *Nanomaterials* **2023**, *13*, 548. [CrossRef] [PubMed]
78. Chatterley, A.S.; Laity, P.; Holland, C.; Weidner, T.; Woutersen, S.; Giubertoni, G. Broadband Multidimensional Spectroscopy Identifies the Amide II Vibrations in Silkworm Films. *Molecules* **2022**, *27*, 6275. [CrossRef]
79. Kacuráková, M.; Capek, P.; Sasinková, V.; Wellner, N.; Ebringerová, A. FT-IR study of plant cell wall model compounds: Pectic polysaccharides and hemicelluloses. *Carbohydr. Polym.* **2000**, *43*, 195–203. [CrossRef]
80. Slavin, Y.N.; Bach, H. Mechanisms of Antifungal Properties of Metal Nanoparticles. *Nanomaterials* **2022**, *12*, 4470. [CrossRef]
81. Ekwomadu, T.I.; Mwanza, M. *Fusarium* Fungi Pathogens, Identification, Adverse Effects, Disease Management, and Global Food Security: A Review of the Latest Research. *Agriculture* **2023**, *13*, 1810. [CrossRef]
82. Lipovsky, A.; Nitzan, Y.; Gedanken, A.; Lubart, R. Antifungal activity of ZnO nanoparticles—the role of ROS mediated cell injury. *Nanotechnology* **2011**, *22*, 105101. [CrossRef]
83. Subba, B.; Rai, G.B.; Bhandary, R.; Parajuli, P.; Thapa, N.; Kandel, D.R.; Mulmi, S.; Shrestha, S.; Malla, S. Antifungal activity of zinc oxide nanoparticles (ZnONPs) on *Fusarium equiseti* phytopathogen isolated from tomato plant in Nepal. *Heliyon* **2024**, *10*, e40198. [CrossRef]
84. Kreuter, J. Influence of the surface properties on nanoparticle-mediated transport of drugs to the brain. *J. Nanosci. Nanotechnol.* **2004**, *4*, 484–488. [CrossRef]